COMMUNICATIONS PHYSICS

ARTICLE

DOI: 10.1038/s42005-018-0005-8 OPEN

Mapping the band structure of GeSbTe phase change alloys around the Fermi level

J. Kellner[1], G. Bihlmayer[2], M. Liebmann[1], S. Otto[3], C. Pauly[1], J.E. Boschker[4], V. Bragaglia[4], S. Cecchi[4], R.N. Wang[4], V.L. Deringer[5,7], P. Küppers[1], P. Bhaskar[1], E. Golias[6], J. Sánchez-Barriga[6], R. Dronskowski[5], T. Fauster[3], O. Rader[6], R. Calarco[4] & M. Morgenstern[1]

Phase change alloys are used for non-volatile random-access memories exploiting the conductivity contrast between amorphous and metastable, crystalline phase. However, this contrast has never been directly related to the electronic band structure. Here we employ photoelectron spectroscopy to map the relevant bands for metastable, epitaxial GeSbTe films. The constant energy surfaces of the valence band close to the Fermi level are hexagonal tubes with little dispersion perpendicular to the (111) surface. The electron density responsible for transport belongs to the tails of this bulk valence band, which is broadened by disorder, i.e., the Fermi level is 100 meV above the valence band maximum. This result is consistent with transport data of such films in terms of charge carrier density and scattering time. In addition, we find a state in the bulk band gap with linear dispersion, which might be of topological origin.

[1] II. Physikalisches Institut B and JARA-FIT, RWTH Aachen University, D-52074 Aachen Germany. [2] Peter Grünberg Institute (PGI-1), Forschungszentrum Jülich, D-52428 Jülich Germany. [3] Lehrstuhl für Festkörperphysik, Universität Erlangen-Nürnberg, D-91058 Erlangen Germany. [4] Paul-Drude-Institut für Festkörperelektronik Berlin, D-10117 Berlin Germany. [5] Institute of Inorganic Chemistry, RWTH Aachen University, D-52074 Aachen Germany. [6] Helmholtz-Zentrum für Materialien und Energie BESSY II, D-14109 Berlin Germany. [7] Present address: Engineering Laboratory, University of Cambridge, Cambridge CB2 1PZ, UK. Correspondence and requests for materials should be addressed to M.M. (email: mmorgens@physik.rwth-aachen.de)

Phase change alloys are the essential components for optical data storage (DVD-RW, Blu-ray Disc) and for electrically addressable phase-change random-access memories (PC-RAM)[1,2]. The latter are envisioned to become more energy efficient using interfacial phase-change memories, whose phase change has been related to a topological phase transition[3]. Phase change alloys are typically chalcogenides consisting of Ge, Sb, and Te (GST) with $Ge_2Sb_2Te_5$ (GST-225) being the prototype[1,4]. They exhibit three different structural phases: an amorphous, a metastable rock salt, and a stable trigonal phase. Switching the system from amorphous to metastable leads to a large contrast in electrical conductivity and optical reflectivity, which is exploited for data storage[5,6]. Such switching favorably occurs within nanoseconds[7,8] and at an energy cost down to 1 fJ for a single cell[9].

The technologically relevant, metastable phase[10], usually obtained by rapid quenching from the melt, has a rock salt like structure with Te atoms at one sublattice and a mixture of randomly distributed Ge, Sb, and vacancies (Vcs) on the other sublattice (Fig. 1a, b)[11–14]. The stable phase consists of hexagonally close-packed layers of either Ge, Sb, or Vcs with hexagonal layers of Te in between. Hence, the Vc layers bridge adjacent Te layers[15,16]. The stable phase has trigonal symmetry and is distinct in stacking of the hexagonal layers from the regular ABC stacking within the rock salt like metastable phase (Fig. 1c, d).

In the metastable phase, the disorder on the (Ge, Sb, and Vc) site leads to Anderson localization of the electrons[17]. The localization is lifted by annealing due to the respective continuous ordering of the Ge, Sb, and Vcs into different layers[18–20]. This is accompanied by a shift of the Fermi level E_F toward the valence band (VB)[17,21]. However, the corresponding Fermi surface is not known, as well as the exact position of E_F, such that it is difficult to understand the electrical conductivity in detail.

Most of the electrical transport measurements so far were conducted using polycrystalline GST[17,22], such that many established tools requiring crystallinity of the samples could not be applied. Only recently, epitaxial films of single-crystalline quality have been achieved by molecular beam epitaxy (MBE)[20,23–26]. These films have been probed so far by X-ray diffraction (XRD), electron microscopy[20,23–27], magnetotransport studies[20], Raman spectroscopy, and Fourier transform infrared spectroscopy[26,28]. Most importantly, it was found that the epitaxial GST films are in the technologically relevant rock salt phase, but often exhibit ordering of the vacancies in separate layers[20].

Here we provide the first detailed measurement of the band structure of such epitaxial films by angular resolved photoelectron spectroscopy (ARPES). We focus on the nominal composition GST-225, and employ an ultrahigh-vacuum (UHV) transfer from the MBE system to prevent surface oxidation[29] (Methods section). Within the whole-Brillouin zone (BZ), we find an M-shaped bulk VB in all directions parallel to the surface. This is in qualitative agreement with density functional theory (DFT) calculations of the cubic adaption of the trigonal Petrov phase[15,30], sketched in Fig. 1d. For brevity, we call this structure the cubic Petrov phase. Connecting the VB maxima of the experimental data results in a hexagonal tube at an energy about 100 meV below E_F. Hence, the classical Fermi volume of a strictly periodic system would be zero, which contradicts the observation of metallic conductivity[20]. This apparent contradiction is solved by the significant broadening of the $E(\mathbf{k})$ states due to disorder, such that there is still considerable weight of the valence band states above E_F. The sum of these weights results in a charge carrier density n_{eff} consistent with the charge carrier density obtained from Hall measurements of the MBE films. The width of the states is, moreover, compatible with the scattering time deduced from the transport data. Such a detailed description of electrical transport provides a significant improvement over more simplistic models based on a parabolic and isotropic valence band as used so far[17,22].

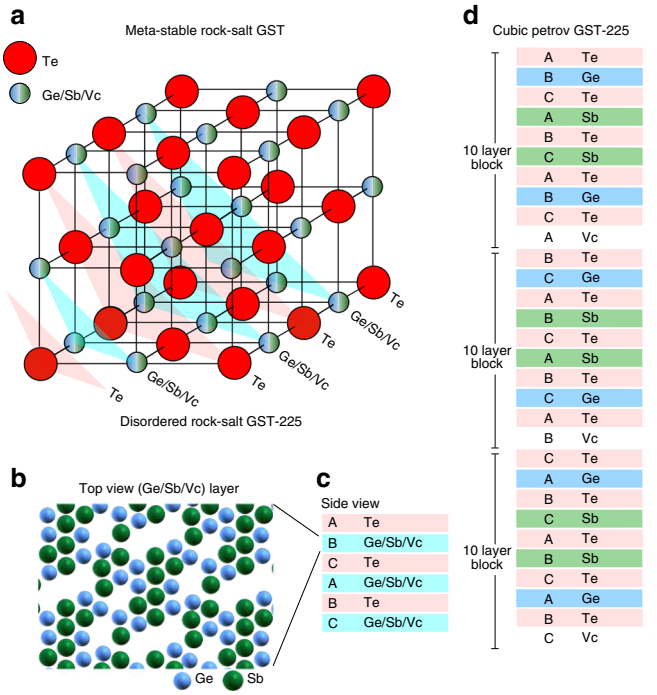

Fig. 1 Structural models of $Ge_2Sb_2Te_5$ (GST-225). **a** Metastable rock salt structure: red circles: Te, striped circles: Ge, Sb, or vacancy (Vc); (111) planes are marked with alternating colors (red: Te, turquoise: Ge/Sb/Vc); **b** DFT-optimized structure of the disordered subsurface layer of a GST-225 slab, blue: Ge, green: Sb; **c** layer structure of one unit cell of metastable rock salt GST-225 exhibiting ABC stacking; the 2 × 3 layers in the unit cell result from the two chemically distinct layers and the three distinct stacking positions; **d** same as **c**, but for the cubic Petrov phase of GST-225 exhibiting a unit cell of 10 × 3 layers with 10 layers due to the alternating chemistry and a threefold repetition due to the ABC stacking

Additionally, we find an electronic band within the fundamental bulk band gap of the metastable phase by two-photon ARPES. This band exhibits a largely isotropic, linear dispersion and circular dichroism, such as known for topological surface states (TSS)[31–33]. We also find states close to the VB maximum with a strong in-plane spin polarization perpendicular to **k** by conventional ARPES again similar to TSSs. A non-trivial topology of GST-225 has indeed been predicted for certain stacking configurations by DFT calculations[34–38] and has been conjectured from the M-type VB dispersion[39]. Assuming that the Dirac-type state is indeed a TSS and, hence, cuts E_F, it would contribute to the electronic transport. It would even dominate the conductivity, if its mobility $\mu > 0.1\ m^2\ (Vs)^{-1}$. This is lower than the best TSS mobilities found in other topological insulators, such as Bi_2Se_3 and $BiSbTeSe_2$ films ($\mu \simeq 1\ m^2\ (Vs)^{-1}$)[40,41].

Results

Constant energy surfaces. ARPES experiments were performed at 29 different photon energies $h\nu = 16$–31 eV with a step size of 0.5 eV. This allows a detailed determination of the k_z dispersion of the bands (k_z: wave vector perpendicular to the surface). Using the estimated crystal potential $E_{inner} = 14$ eV (Methods section), the chosen $h\nu$ relate to $k_z = 2.55$–$3.09\ Å^{-1}$. The ARPES spectra show an inverted M-shaped VB in energy-momentum cuts (EMCs) taken along the surface plane (Fig. 2d). The independently measured Fermi level E_F^{PES} is well above the VB maximum.

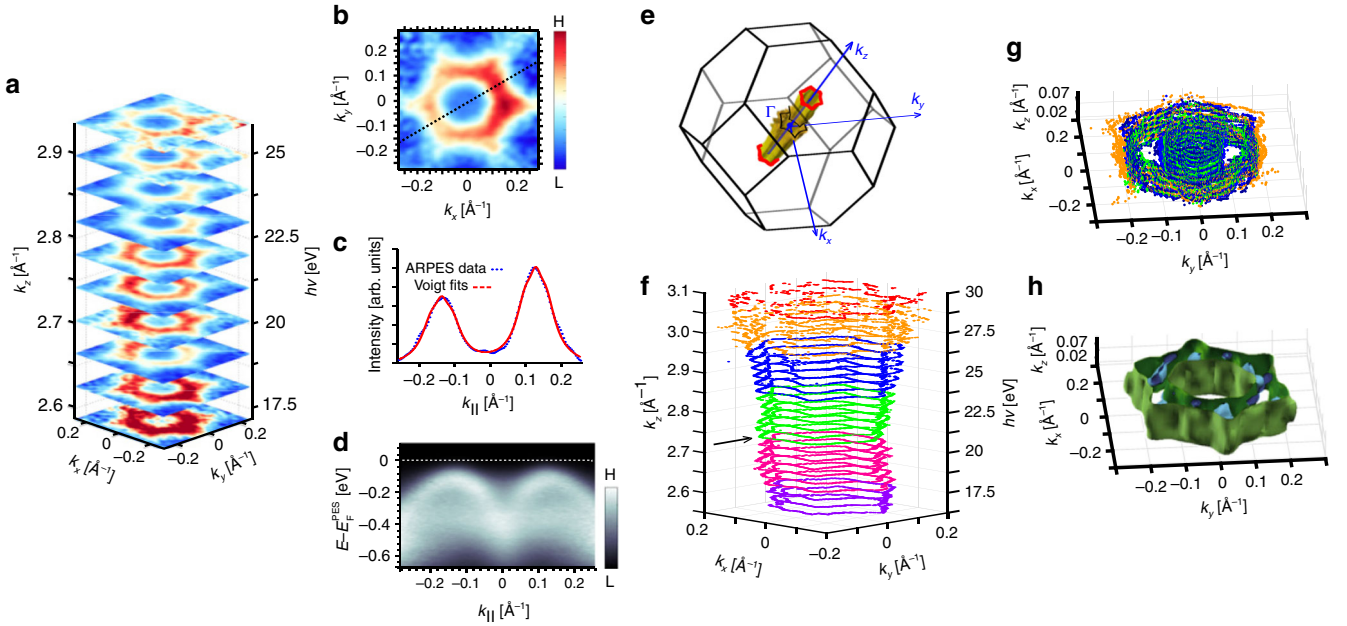

Fig. 2 ARPES and DFT data for different photon energies $h\nu$. **a** Constant energy cuts (CECs) at the Fermi level E_F^{PES} for different $h\nu$. We deduce k_z as marked on the left from $h\nu$ using an inner potential $E_{inner} = 14$ eV (Methods section); **b** CEC at E_F^{PES} for $k_z = 2.83$ Å^{-1} with direction equivalent to k_y marked by a dotted black line; **c** momentum distribution curve (MDC) along dotted black line in **b**; two Voigt peaks (red line) are fitted to the ARPES data (blue dots); **d** Energy-momentum cut (EMC) along the dotted line marked in **b** at $k_z = 2.83$ Å^{-1}, dashed line marks E_F^{PES}; **e** Brillouin zone (BZ) of metastable, disordered rock salt GST-225 (structure in Fig. 1a) with principal **k** directions marked; the measured pseudo Fermi surface is shown in gold, including the missing part due to vanishing photoelectron intensity (Methods section); the Fermi lines cutting the BZ side planes in (111) direction are drawn in red; **f** Voigt peak positions at E_F^{PES} from MDC fits as in **c**; colors are alternating in $\Delta k_z = 0.12$ Å^{-1}, being the k_z size of the BZ of the cubic Petrov phase as used in the DFT calculations; the tentative BZ boundary of the metastable rock salt phase at $k_z = 2.72$ Å^{-1} is marked by a black arrow; it is used to determine E_{inner}; the additionally given photon energies (right scale) correspond to the average diameter of the hexagons; **g** $E_{peak,1}$ (**k**) at $E - E_F^{PES} = -200$ meV after backfolding along k_z into the BZ of the cubic Petrov phase (same color code as in **f**); **h** constant energy surfaces (CESs) of the valence bands (VBs) of the cubic Petrov phase according to DFT at the experimental $E - E_F^{PES} = -200$ meV, i.e., after shifting E_F^{DFT} by 100 meV upward, such that the VB maxima in DFT and ARPES match

Both are in line with earlier, less extensive results[39]. We label E_F^{PES} additionally with the superscript PES, since it differs from E_F^{DFT} in DFT calculations with respect to the VB maximum. Figure 2a displays constant energy cuts (CECs) of the normalized photoelectron intensity (methods) at E_F^{PES} for selected k_z. To determine peak positions, momentum distribution curves (MDCs) are extracted and fitted by Voigt peaks (Fig. 2b, c). The resulting peak momenta **k** form a hexagonal tube (Fig. 2e, f) called the pseudo Fermi surface of GST-225. We call it pseudo, since the peak energies E_{peak}(**k**) resulting from fits of energy distribution curves (EDCs) do not cross E_F^{PES} for any **k**, as visible, e.g., in Fig. 2d. Consequently, there are no band centers at E_F^{PES} as required for a conventional Fermi surface[42]. Only the tails of the broadened energy peaks cross E_F. The sizes of the hexagons of the pseudo Fermi surface slightly vary with $h\nu$, i.e., along k_z, with minimal diameter at $h\nu = 21$ eV (arrow in Fig. 2f). We conjecture (in accordance with DFT) that this minimum corresponds to the BZ boundary and, hence, use it to determine $E_{inner} = 14$ eV, unambiguously relating $h\nu$ to k_z (Methods section). For the Fermi wave number in x (y) direction, we find $k_{F,x} = 1.52 \pm 0.3$ nm^{-1} ($k_{F,y} = 1.43 \pm 0.2$ nm^{-1}), where the ± interval describes the full variation along k_z. Hence, with a precision of 20%, the pseudo Fermi surface is a hexagonal tube without dispersion along k_z.

The EDCs consist of up to two peaks down to $E - E_F^{PES} = -1$ eV for all probed **k**. These peaks are fitted by two Voigt peaks with peak centers $E_{peak,j}$(**k**) ($j = 1, 2$). The highest peak energy for all **k**, i.e., the VB maximum, is found at $E_{peak,1}$(**k**) $- E_F^{PES} = -105 \pm 10$ meV with **k** = (0 ± 0.02, 1.53 ± 0.02, and 25.8 ± 0.2) nm^{-1}, as well as at equivalent **k** points. Projecting back to the first BZ, we get **k** = (0, 1.53, 1.6) nm^{-1}, i.e., the VB maximum is offset from Γ also in k_z direction.

Constant energy surfaces (CESs) of $E_{peak,j}$(**k**) are constructed below the VB maximum[42–45]. They are compared with CESs from DFT calculations, which require periodic boundary conditions, i.e., a distinct order within the Ge/Sb/Vc layer. We have chosen the cubic Petrov phase (Fig. 1d) to represent the metastable ABC stacking of the rock salt structure employing chemically pure Sb, Ge, and Vc layers[30,39]. Since the corresponding DFT BZ is reduced in k_z direction by a factor of 5 with respect to the disordered rock salt phase (Fig. 1a–c), the ARPES data have to be back-folded into a k_z range of $\Delta k_z = 0.12$ Å^{-1} for comparison. Therefore, the measured k_z data are divided into parts covering $\Delta k_z = 0.12$ Å^{-1} each (see color code in Fig. 2f) and projected accordingly. Results at $E - E_F^{PES} = -200$ meV are shown in Fig. 2g, where each MDC has been fitted by four Voigt peaks as exemplary shown in Fig. 3g. The qualitative agreement with the DFT CESs (Fig. 2h) is reasonable, in particular, for the outer hexagon. Such agreement is also found at other energies as shown in Fig. 3a–f, where the different k_z values are projected to the (k_x, k_y) plane. However, quantitative differences are apparent as discussed in Supplementary Note 1.

Effective charge carrier density from ARPES and magneto-transport. Next, we deduce the effective charge carrier density n_{eff} from the detailed mapping of the VBs by ARPES. Since the VB maximum is found 105 meV below E_F^{PES} (Fig. 2d), one might conjecture the absence of a Fermi surface, i.e., $n_{eff} = 0$, at least close to the surface, i.e., at the origin of the ARPES signal. However, the bands are significantly broadened, such that their tails cut E_F^{PES} (Fig. 2). Hence, the tails of the VB give rise to a

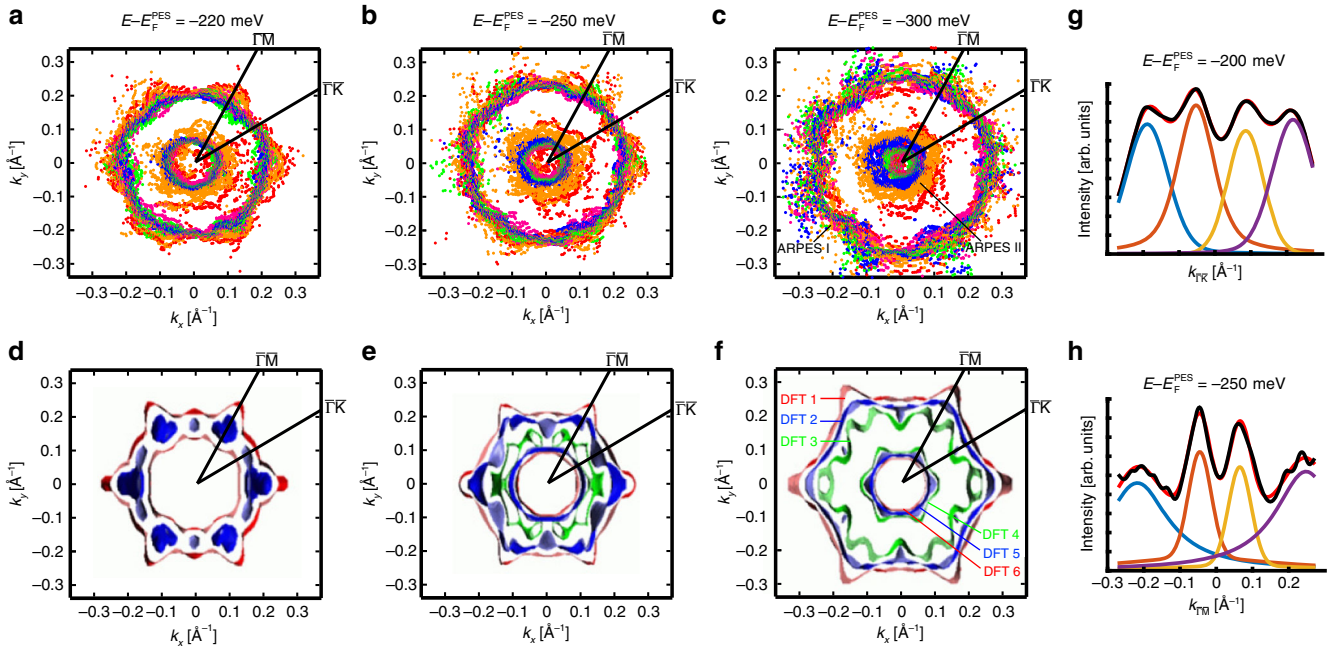

Fig. 3 Comparison between ARPES and DFT at different binding energies $E - E_F^{PES}$. **a**–**c** Voigt peak positions $E_{peak,1}(\mathbf{k})$, deduced from MDC fittings, projected to the (k_x, k_y) plane; the marked $\overline{\Gamma M}$ and $\overline{\Gamma K}$ belong to a surface BZ projection; the color code is the same as in Fig. 2f-g; **d**–**f** corresponding CESs from DFT calculations exhibiting three Sb p-type VBs (different colors) within the BZ of the cubic Petrov phase; numberings in **c** and **f** label the different bands; **g**, **h** measured MDCs (black curves) along $\mathbf{k}_{||}$ directions and at $E - E_F^{PES}$ as marked. Red fit curves consist of the displayed four Voigt peaks (blue, orange, yellow, and violet curve)

Table 1 Magnetotransport data

$n_{eff,H}$ (10^{26} m^{-3})	σ_{xx} (S m^{-1})	μ (m^2(Vs)$^{-1}$)	d (nm)
0.13	2.700	0.0013	19
0.26	4.000	0.0010	28
3.0	60.000	0.0012	23

Charge carrier density $n_{eff,H}$, longitudinal conductivity σ_{xx}, and mobility μ, as determined by 4-point magnetoconductance measurements at $T = 300$ K, as well as thickness d for different epitaxial GST-225 films

non-vanishing n_{eff}. Accordingly, we replace the usual

$$n_{\mathrm{eff}} = \frac{2}{8\pi^3} \iiint_{\text{Fermi volume}} \mathrm{d}^3\mathbf{k}, \qquad (1)$$

where the Fermi volume includes all occupied states, with:

$$n_{\mathrm{eff}} = \frac{2}{8\pi^3} \sum_j \iiint_{\mathrm{BZ}} \alpha_j(\mathbf{k})\, \mathrm{d}^3\mathbf{k}. \qquad (2)$$

The integral covers the whole BZ and includes the weight of each state above E_F^{PES} (inset of Fig. 4a) according to

$$\alpha_j(\mathbf{k}) = \int_{E_F^{PES}}^{\infty} p_{j,\mathrm{norm}}(E,\mathbf{k})\mathrm{d}E. \qquad (3)$$

Here, $p_{j,norm}$ (E, $\mathbf{k}$) is the fitted EDC peak at $\mathbf{k}$ of band j, after normalizing its area to unity.

Figure 4a shows an exemplary EDC (black points) fitted with two Voigt peaks $p_j(E, \mathbf{k})$ (blue and green line), which are multiplied by the Fermi distribution function $f_0(E, T)$ at $T = 300$ K (thin, red line). This provides an excellent fitting result (thick red line). The weights of the two peaks above E_F are evaluated to be $\alpha_1(\mathbf{k}) = 3\%$ and $\alpha_2(\mathbf{k}) = 1\%$ (inset of Fig. 4a) (Methods section). Generally, we find $\alpha_1(\mathbf{k}) \leq 7\%$ for 97% of the EDCs, where the largest $\alpha_1(\mathbf{k})$ are coincident with the maxima of $E_{peak}(\mathbf{k})$. This is illustrated in the inset of Fig. 4d showing $\alpha_1(\mathbf{k})$ and $\alpha_2(\mathbf{k})$ for the EMC of Fig. 4b.

We only evaluate the contributions of the two upper VBs (p_1, p_2), since all other bands are >1 eV below E_F^{PES}. Then, the α_j ($\mathbf{k}$) for different $\mathbf{k}$ are summed up and multiplied by 1.25 in order to compensate for the part of the BZ, which is not probed by ARPES. Finally, we normalize appropriately. This eventually leads to $n_{eff} = (4.4 \pm 1.1) \times 10^{26}$ m^{-3} with uncertainty resulting from the individual error bars of peak energies and peak widths within the Voigt fits. Taking only the contributions from the upper peak p_1, we get $n_{eff,1} = (2.6 \pm 0.6) \times 10^{26}$ m^{-3}. Since the surface might be influenced by band bending, we also calculated n_{eff} for an artificially varying E_F with respect to the measured E_F^{PES} as displayed in Fig. 4d.

Next, we compare these n_{eff} with the results from Hall measurements, which yields the bulk charge carrier density $n_{eff,H} = e\sigma_{xy}/B$ (σ_{xy}: Hall conductivity, B: magnetic field) varying between 1.3×10^{25} m^{-3} and 3.0×10^{26} m^{-3} for nominally identical samples (Table 1). The variation is probably caused by the known, strong sensitivity of GST transport properties to disorder[17]. The temperature dependence of σ_{xy} is small within the interval $T =$ 4–300 K (changes <10%) demonstrating metallic conductivity. The interval of the $n_{eff,H}$ data is marked in Fig. 4d. The larger $n_{eff,H}$ excellently match $n_{eff}(E_F^{PES})$, while the smaller ones are compatible with an E_F shifted further upward. In any case, the tails of the VB provide enough density of states to host the charge carrier density $n_{eff,H}$. We conclude that E_F of GST-225 is indeed well above the VB maximum. In turn, we can estimate the required n_{eff} to locate E_F at the VB maximum ($E - E_F^{PES} = -105$ meV) to be $n_{eff} \simeq 3 \times 10^{27}$ m^{-3} ($n_{eff,1} \simeq 2.3 \times 10^{27}$ m^{-3}), i.e., an order of magnitude larger than the highest values found by the Hall measurements. This excludes a significant downward band bending of the VB toward the surface.

In principle, one could argue that the peak width is not due to disorder, but due to the finite lifetime of the photo-hole produced by ARPES[43,44]. However, the Voigt fits, which add up a Gaussian peak and a Lorentzian peak, exhibit, on average, 99% (97%)

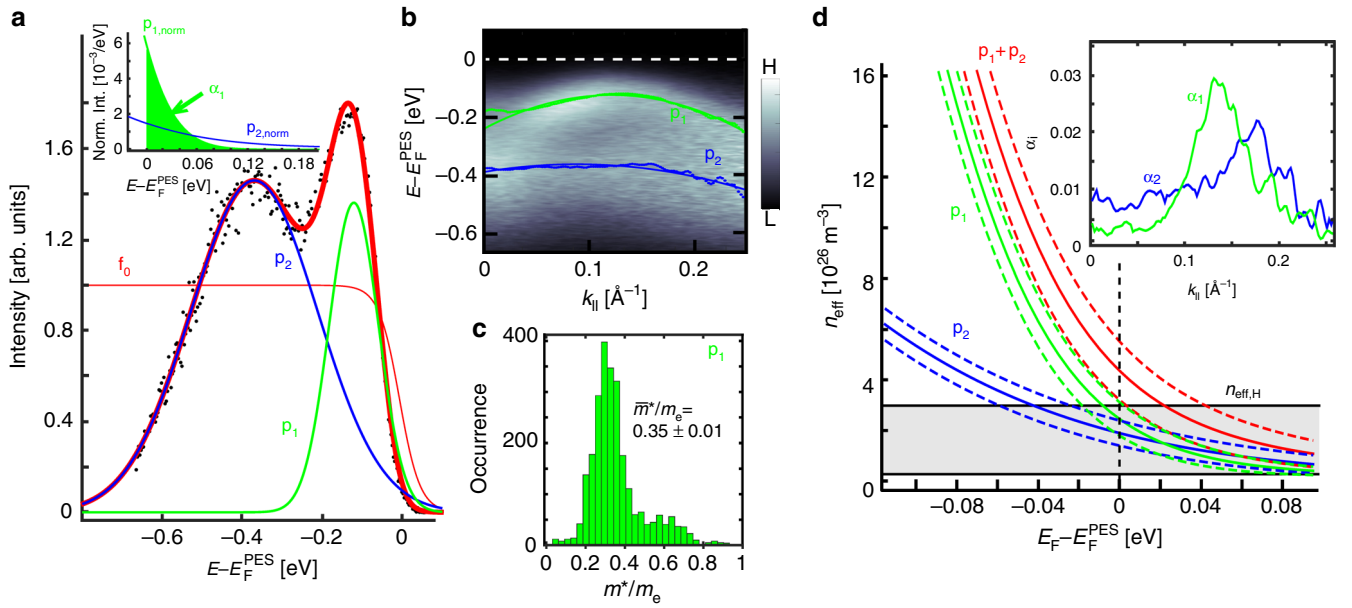

Fig. 4 Charge carrier density n_{eff} and curvature parameter $m^\star$ deduced from ARPES. **a** EDC at $\mathbf{k} = (0.0, 0.13, 2.73)$ Å^{-1} (black dots) with fit curve (red) consisting of two Voigt peaks (p_1 = green, p_2 = blue) multiplied by the Fermi distribution function f_0 (E, T = 300 K) (thin red line); inset: zoom around E_F^{PES} displaying peak tails, after scaling each peak area to unity; only the colored tail of peak 1 (marked α_1) contributes to $n_{eff,1}$; **b** EMC at $k_z = 2.73$ Å^{-1} with marked peak positions p_1 (green dots) and p_2 (blue dots) resulting from fits of EDCs as in **a**; parabolic fits to these points (accordingly colored full lines), used to determine $m^\star$, are added; **c** histogram of resulting $m^\star/m_e$ belonging to the band of p_1 using 90 different azimuths in (k_x, k_y) direction for 29 different k_z-values; errors for individual $m^\star/m_e$ are about the bin width; **d** red full line: n_{eff} as calculated from the ARPES data according to Eq. (2) for a hypothetically varying E_F with respect to the measured E_F^{PES}; different contributions from p_1 (green full line) and p_2 (blue full line) are labeled; error intervals are depicted by correspondingly colored dashed lines; charge carrier densities from Hall measurements ($n_{eff,H}$) of identically prepared GST films are added as a gray box; inset: α_j (**k**) (relative part of the Voigt peak p_j at **k** above E_F^{PES}) for the EMC of **b**

Gaussian contribution and 1% (3%) Lorentzian contribution for p_1 (p_2). Therefore, the lifetime broadening, encoded in the Lorentzian part, is negligible[43,44]. Moreover, the average electron scattering time $\overline{\tau}$ detected by magnetotransport reasonably fits to the disorder-induced peak widths (see below).

Electron mean free path from ARPES and magnetotransport. Next, we deduce the average scattering lifetime of the electrons ($\overline{\tau}$) and the average mean free path $\overline{\lambda}_{MFP}$ from the combination of ARPES and magnetotransport. In Supplementary Note 2, we show that the longitudinal conductivity σ_{xx} and σ_{xy} can be straightforwardly related to $\overline{\tau}$ for an isotropic, M-shaped parabolic band in (k_x, k_y) direction with negligible dispersion in k_z direction and without peak broadening. Thus, in line with the ARPES data, we approximate the dispersion as

$$E_{peak}(\mathbf{k}) = E_{peak,0} - \frac{\hbar^2}{2m^\star}\left(k_{||} - k_0\right)^2 \qquad (4)$$

with ($E_{peak,0}$, k_0) being the cusp of the inverted parabola and $m^\star := \hbar^2\left(\mathrm{d}^2E/\mathrm{d}k_{||}^2\right)^{-1}$ representing the curvature in radial in-plane direction. This $m^\star$ is different from a universal effective mass of the VB, since the band curvature differs for other **k** directions. We obtain (Supplementary Note 2):

$$\sigma_{xx} = \frac{e^2 n_{eff}\overline{\tau}}{2m^\star} \qquad (5)$$

$$\sigma_{xy} = en_{eff}/B, \qquad (6)$$

with σ_{xx} being distinct by a factor of 1/2 from the standard Drude result, which is only valid for an isotropic, parabolic band centered at Γ. To determine $\overline{\tau}$, we have, hence, to deduce $m^\star$ from ARPES, besides n_{eff}. Corresponding parabolic fits to $E_{peak,1}$ (**k**), exemplary shown in Fig. 4b, are executed for all EMCs at different azimuths in (k_x, k_y) direction and different k_z. This leads to the histogram of $m^\star$ values in Fig. 4c with mean $\overline{m}^\star = (0.35 \pm 0.01) \cdot m_e$ (m_e: bare electron mass, Table 2).

During the same fit, we naturally get an average k_0 as given in Table 2 ($\overline{k}_0$) and an average $E_{peak,0}$ being $\overline{E}_{peak,0} - E_F^{PES} = -122 \pm 3$ meV. With the determined $\overline{m}^\star$, we can use magnetotransport data and Eq. (5) to estimate $\overline{\tau}$. For the sample, where $n_{eff,H}$ fits best to n_{eff} from ARPES (Table 1), we measured $n_{eff,H} = (3.0 \pm 0.2) \times 10^{26}$ m^{-3} and $\sigma_{xx} = (6 \pm 1) \times 10^4$ S m^{-1} (at 300 K) leading to $\overline{\tau} = 5 \pm 1$ fs (Table 3). The variation between different samples grown with the same parameters (Methods section, Table 1) is negligible.

Straightforwardly, we can determine other parameters of the dispersion of Eq. (4), including the Fermi wave vector $\overline{k}_F$ and the Fermi velocity $\overline{v}_F$, while still neglecting the peak broadening (Supplementary Note 2):

$$E_F - \overline{E}_{peak,0} = -\frac{\hbar^2}{8\overline{m}^\star}\left(\frac{\pi c n_{eff}}{\overline{k}_0}\right)^2 = -(12 \pm 1)\ \mathrm{meV} \qquad (7)$$

$$\left|\overline{k}_F - \overline{k}_0\right| = \sqrt{\frac{2\overline{m}^\star\left|E_F - \overline{E}_{peak,0}\right|}{\hbar^2}} = (0.34 \pm 0.02)\ \mathrm{nm}^{-1} \qquad (8)$$

$$\overline{v}_F = \frac{\hbar}{\overline{m}^\star}\left|\overline{k}_F - \overline{k}_0\right| = \frac{\pi\hbar}{2\overline{m}^\star} \cdot \frac{c n_{eff}}{\overline{k}_0} \qquad (9)$$

$$= (1.1 \pm 0.1) \times 10^5\ \mathrm{m\,s^{-1}} \qquad (10)$$

$$\overline{\lambda}_{MFP} = \overline{v}_F \cdot \overline{\tau} = \frac{\pi\hbar c}{e^2\overline{k}_0} \cdot \sigma_{xx} = (0.6 \pm 0.1)\ \mathrm{nm}, \qquad (11)$$

Table 2 VB parameter of epitaxial GST-225

$\overline{m}^\star/m_e$	$\overline{k}_0$ (nm^{-1})	c (nm)	$n_{eff,H}$ (10^{26} m^{-3})
0.35 ± 0.01	1.47 ± 0.02	1.04	0.13–3.0

$\overline{m}^\star$: curvature parameter, $\overline{k}_0$: average position of the cusp of the M-type VB in (k_x, k_y) direction, c: size of the unit cell of the disordered, cubic Petrov phase along the direction perpendicular to the layers[63], $n_{eff,H}$: charge carrier density interval according to Hall measurements

Table 3 Comparison of scattering time and connected parameters derived from simple and full model

	Simple model	Full model
$\overline{\tau}$ in fs	5 ± 1	3 ± 1
$\overline{v}_F$ in m s^{-1}	(1.1 ± 0.1) × 10^5	(1.2 ± 0.1) × 10^5
$\overline{\lambda}_{MFP}$ in nm	0.6 ± 0.1	0.4 ± 0.1

Averaged scattering time $\overline{\tau}$, averaged Fermi velocity $\overline{v}_F$ at E_F^{PES} and resulting average mean free path $\overline{\lambda}_{MFP}$ for the sample with charge carrier density $n_{eff} = (3.0 \pm 0.2) \times 10^{26}$ m^{-3} and conductivity $\sigma_{xx} = (6 \pm 1) \times 10^4$ Sm^{-1}. The values are deduced within a simple model neglecting the disorder-induced peak broadening and the variation of $m^\star$ across the BZ and within the full model taking both aspects into account

where $c = 1.04$ nm (Table 2) is the length of the unit cell of the metastable rock salt phase (structure model in Fig. 1a–c) perpendicular to the layers. The numerical values are again given for the sample with $n_{eff} = (3.0 \pm 0.2) \times 10^{26}$ m^{-3} and $\sigma_{xx} = (6 \pm 1) \times 10^4$ S m^{-1} (Table 1). E_F is located in the band belonging to p_1 for all $n_{eff,H}$ of our samples. Note that neither $\overline{m}^\star$, as usual, nor n_{eff}, as typical for two-dimensional (2D) systems[46], enters the evaluation of $\overline{\lambda}_{MFP}$, but only $\overline{k}_0$ does. This reflects the dominating 2D-type dispersion for GST-225.

We also used a more refined, numerical calculation, which considers the variation of $m^\star$ across the BZ and the peak broadening, i.e., the fact that E_F^{PES} is above the VB maximum, explicitly. Therefore, we use the low-temperature limit of Boltzmann's relaxation model. We assume that the scattering time τ_j (**k**) does not depend on **k** and band index j, reading $\overline{\tau} := \tau_j(\mathbf{k})$ which leads to

$$\sigma_{xx} = \frac{-e^2}{4\pi^3} \iiint \sum_{j=1}^{2} v_{x,j}^2(\mathbf{k}) \tau_j(\mathbf{k}) p_{j,n}(E,\mathbf{k}) \frac{\mathrm{d}f_0(E(\mathbf{k}),T)}{\mathrm{d}E} d^3\mathbf{k} \quad (12)$$

$$= \frac{\overline{\tau} e^2}{4\pi^3} \iiint \sum_{j=1}^{2} v_{x,j}^2(\mathbf{k}) p_{j,n}(E,\mathbf{k}) \delta(E(\mathbf{k}) - E_F) \mathrm{d}^3\mathbf{k}. \quad (13)$$

The group velocity $\mathbf{v}_j(\mathbf{k})$ is determined from the ARPES data as $\mathbf{v}_j(\mathbf{k}) = \nabla_{\mathbf{k}} E_{peak,j}(\mathbf{k})/\hbar$ with the derivative taken at $E_{peak,j}$ and not at E_F^{PES}. Since the results now depend critically on E_F, we restrict the analysis to the sample with $n_{eff} \simeq n_{eff,H}$ as used in Eq. (7). Numerically, we obtain $\overline{\tau} = 3 \pm 1$ fs, which is nearly a factor of two smaller than within the simplified calculation. By the same numerical $p_{j,n}$ (E, **k**) weighting, we determine the average group velocity at E_F^{PES} as $\overline{v}_F = (1.2 \pm 0.1) \times 10^5$ m s^{-1} leading to $\overline{\lambda}_{MFP} \simeq \overline{v}_F \cdot \overline{\tau} = 0.4 \pm 0.1$ nm (Table 3).

We compare the results of the refined model and the simplified model (Eqs. (5) and (7)) in Table 3 revealing that the simplified model returns reasonable values, but deviates from the more exact, refined model by up to 40%. This must be considered for the interpretation of magnetotransport data, where Eqs. (5) and (7) provide only reasonable estimates for n_{eff}, $\overline{v}_F$, $\overline{\tau}$, and $\overline{\lambda}_{MFP}$ with an intrinsic error of about 40%.

Finally, we comment on the peak width, which is, on average, $\Delta\overline{E}_1 = 0.20 \pm 0.03$ eV (FWHM) for the band p_1. This can be compared with $\Delta\overline{E}_1 \sim \hbar/\tau$ (Supplementary Note 3). We find $\hbar/\Delta\overline{E}_1 = 3.5$ fs in excellent agreement with $\overline{\tau} = 3$ fs as deduced from the transport data of the sample with highest conductivity (largest $\overline{\tau}$) (Table 3). This corroborates the assignment of the peak widths to disorder broadening, as already conjectured from its dominating Gaussian shapes. The fact that σ_{xx} increases by only 15% between room temperature and $T = 4$ K[20] additionally shows that $\overline{\tau}$ is dominated by disorder scattering. We conclude that disorder broadening is responsible for the peak widths within the E(**k**) spectral function of the upper valence band of GST-225. The relatively large peak widths (0.2 eV) allows the Fermi level to be well above all peak maxima, i.e., the charge carrier density fits into the tails of the bands. We finally stress that the peak broadening is not the origin of the p-type doping, which has been found previously to be dominated by excess vacancy formation[47,48].

In-gap surface state. Motivated by our previous finding, that an M-shaped VB with maxima away from high-symmetry points is only compatible with DFT calculations of GST exhibiting non-trivial topology[39], we searched for a surface state within the fundamental band gap. We found such a state by two-photon ARPES (2P-ARPES) exhibiting a linear, largely isotropic dispersion, as well as helical, circular dichroism. The state is probably connected to a strongly spin-polarized state at the VB maximum revealed by spin polarized ARPES (S-ARPES).

Optical measurements revealed a band gap of GST-225 of $E_{gap} \simeq 0.5$ eV in rough agreement with DFT data[49], which was recently corroborated by scanning tunneling spectroscopy ($E_{gap} = 0.45 \pm 0.05$ eV)[39,50,51]. Hence, we have to probe this energy interval above the VB maximum, which does not contain bulk states. We employed laser-based 2P-ARPES at pump energy $h\nu = 1.63$ eV and probe energy $h\nu = 4.89$ eV, hence, populating states in the bulk band gap and in the lower part of the conduction band by the pump pulse, which are subsequently probed by ARPES using the probe pulse. The time delay $\Delta t = 1.33$ ps is chosen to optimize the contrast of the states within the bulk band gap. The EMC in Fig. 5a reveals a strong band above $E - E_F^{PES} = 350$ meV, which we attribute to the bulk conduction band (CB) at 450 meV above the VB maximum. Below this CB, a mostly linearly dispersing band faintly appears (arrows). Corresponding CECs (Fig. 5b) exhibit a largely circular structure of this band in the (k_x, k_y) plane increasing in diameter with increasing energy. The linear dispersion of the band is deduced by applying two Voigt fits to each MDC as shown for two examples in Fig. 5c. The resulting $E_{peak}(|\overline{\mathbf{k}}|)$ (points), averaged along k_x and k_y, are fitted using $E_{peak}(|\overline{\mathbf{k}}|) = E_{peak,D} \pm \hbar v_D k_{||}$ (red and blue line). This reveals a presumable band crossing at $E_{peak,D} - E_F^{PES} = 160 \pm 10$ meV and a band velocity $v_D = (3.8 \pm 0.3) \times 10^5$ m s^{-1}.

Due to the relatively strong one-photon background (Methods section), we could not evaluate the 2P-ARPES signal at lower $E - E_F^{PES}$, such that the presumable crossing point was not probed directly. However, all signatures of this band are compatible with a TSS with mostly linear dispersion.

In addition, we probed the circular dichroism (CD) by 2P-ARPES using a linearly polarized pump and a circular polarized probe pulse[52]. The CD intensity is the scaled difference of photoelectron intensity after clockwise and counterclockwise circular polarization of the probe. It is known that the CD cannot be directly assigned to a spin polarization of initial states[32], but is likely related to an interplay of spin and orbital textures[53]. In our case, it shows a sign inversion with the sign of **k** (Fig. 5d). The opposite inversion is found within the CB and the upper VB, the

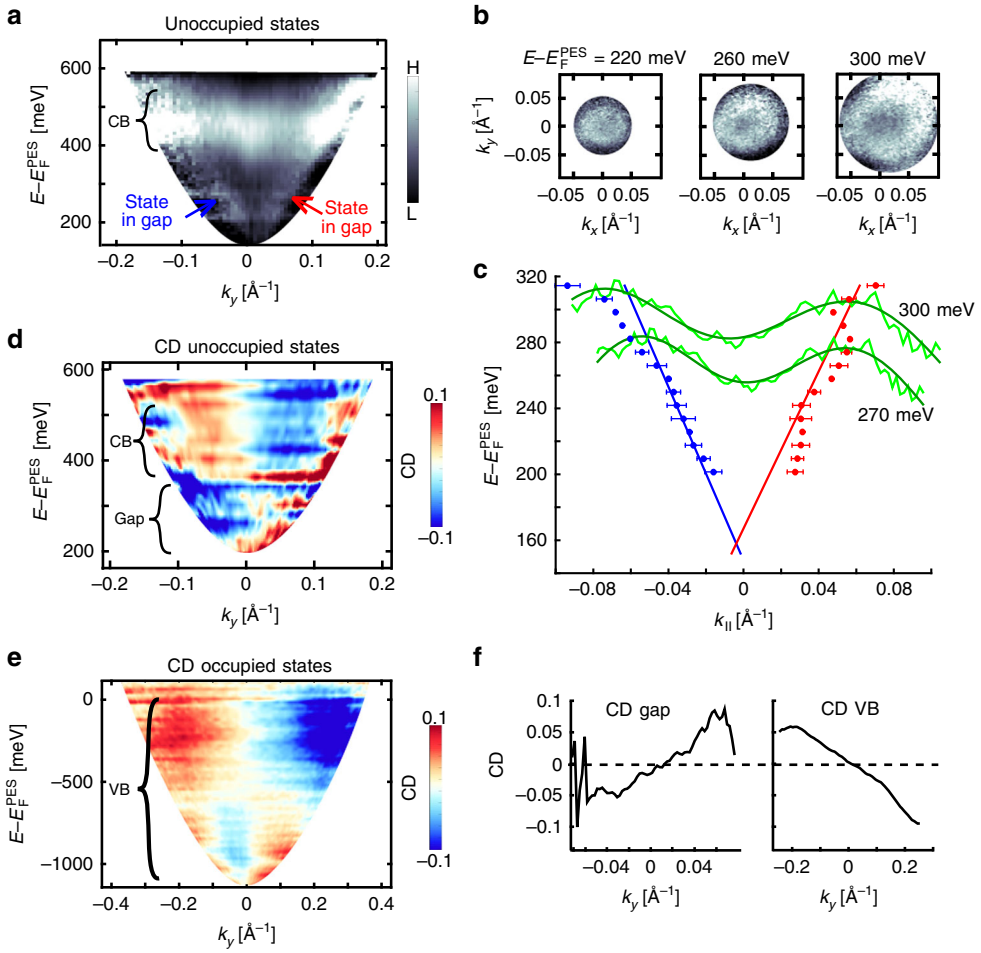

Fig. 5 Two-photon ARPES. **a** EMC of unoccupied states with energy regions of conduction band (CB) highlighted and presumable topological surface state (state in gap) marked by arrows; **b** CECs within the bulk band gap for different $E - E_F^{PES}$ as indicated; **c** green lines: MDCs along k_y at $E - E_F^{PES}$ as marked (jagged lines) with fits consisting of two Voigt peaks (smooth lines); red, blue dots: peak positions of MDC Voigt fits averaged for the MDCs along k_x and k_y; red, blue lines: linear fits to the red and blue dots; **d** circular dichroism (CD) intensity of the 2P-ARPES data of **a** with CB and bulk band gap region (gap) marked; **e** CD intensity of the VB states recorded by one photon ARPES; **f** CD intensity after energy integrating: left: $E - E_F^{PES} = 200$–350 meV from **d**, right: $E - E_F^{PES} = -580$–0 meV from **e** (VB)

latter probed by CD measurements of conventional ARPES (Fig. 5e). The same sequence of CD inversions between VB, TSS, and CB has been found for the prototype strong topological insulators Bi_2Se_3[31], Bi_2Te_3[31,32], and Sb_2Te_3[33], which is an additional hint that the linearly dispersing state within the bulk band gap is a TSS.

Another fingerprint of non-trivial surface states is spin polarization[54–56]. Such spin polarized surface states have been predicted by DFT calculations of the cubic Petrov phase of GST-225, in particular, a TSS traversing the band gap and a Rashba-type surface state at $E - E_F^{PES} = -300\ldots -700$ meV[39]. To this end, we probe the spin polarization of the occupied states at a selected pair of in-plane wave vectors $\pm\mathbf{k}_{||,1}$ (Fig. 6). We choose $h\nu = 30$ eV such that the CEC of the bulk VB is large in diameter (Fig. 2f), thereby increasing the possibility to probe a surface state in the inner part of the BZ, where DFT of the cubic Petrov phase predicted the presence of a TSS[39]. Moreover, we used $|\mathbf{k}_{||,1}| = 0.17 \pm 0.04$ Å^{-1}, large enough to avoid overlap of intensity from $\mathbf{k}_{||,1}$ and $-\mathbf{k}_{||,1}$, thereby getting along with the typically reduced angular resolution of S-ARPES. Indeed, we find strong in-plane spin polarization of 40% close to E_F^{PES} (Fig. 6b, c). The spin polarization inverts sign with the sign of the in-plane wave vector and is perpendicular to $\mathbf{k}_{||,1}$ within error bars (Fig. 6c, d). The other spin polarized state at lower $E - E_F^{PES} = -0.5\ldots -1.2$ eV might be related to the Rashba state mentioned above, which has similarly been found, e.g., for $Sb_2Te_3(0001)$[57].

The peak energy of the spin polarized state close to E_F^{PES} is $E_{peak} - E_F^{PES} = -120 \pm 40$ meV (Fig. 6b), i.e., very close to the VB maximum, such that likely the spin-polarized state extends into the band gap. The error mostly comes from the different peak energies at + $\mathbf{k}_{||,1}$ and $-\mathbf{k}_{||,1}$. We cannot prove that this state is connected to the linearly dispersing state of Fig. 5, which would hit the VB maximum at $|\mathbf{k}_{||}| = 0.10$ Å^{-1}, if perfectly linear in dispersion down to the VB, but we believe that this is likely.

One might ask why such a linearly dispersing state is not observed in the one-photon ARPES data. A possible explanation is the fact that a surface state will follow the roughness of the surface, which for our films amounts to angles of 0.5°–3° according to atomic force microscopy[39]. Assuming, for the sake of simplicity, the same state dispersion on all surfaces, this results in a $k_{||}$ broadening of the surface state by (0.15–1.5) nm^{-1} for $E_{kin} =$ 12–27 eV. The widths of the 2P-ARPES peaks in Fig. 5c is 0.6 nm^{-1} and, hence, well compatible with this analysis. Since the bulk states are not influenced by this broadening mechanism, it gets rather difficult to discriminate the TSS in the presence of bulk VB states at similar $E(\mathbf{k})$ as within our one-photon ARPES data.

We did not reproduce the dispersion of the found state in the bulk band gap by the DFT calculations of slabs of the cubic Petrov

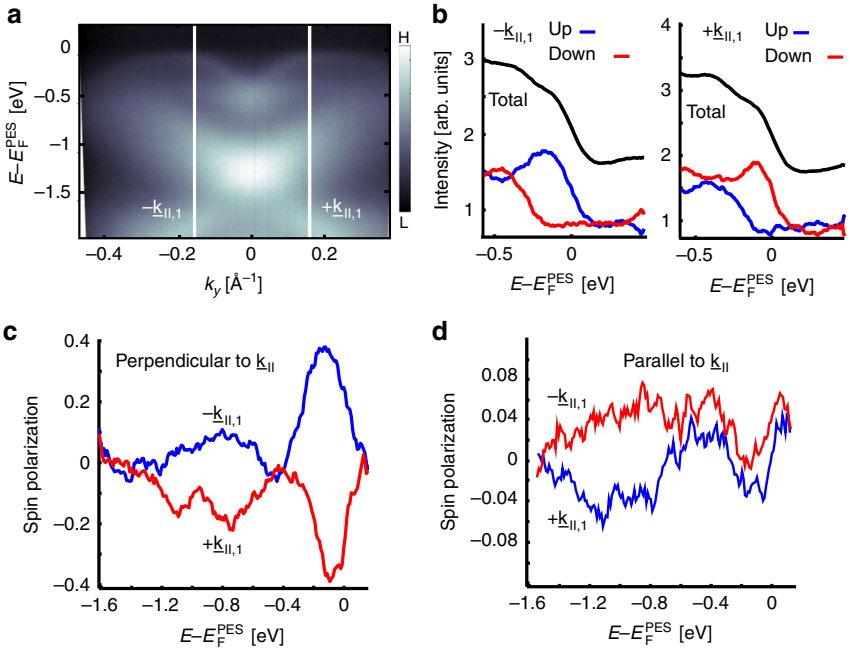

Fig. 6 Spin polarized ARPES. **a** ARPES spectrum along k_y (ΓK) at $h\nu = 30$ eV; labeled white lines mark the k_y positions for the spin resolved measurements in **b**–**d**; **b** recorded in-plane signal of the spin up (blue curve) and spin down (red curve) channel perpendicular to $\mathbf{k}_{\parallel,1}$ after scaling with the Sherman function; black line: sum of red and blue line; left: $-\mathbf{k}_{\parallel,1}$, right: $+\mathbf{k}_{\parallel,1}$; **c** resulting in-plane spin polarization perpendicular to $\mathbf{k}_{\parallel,1}$; **d** in-plane spin polarization parallel to $\mathbf{k}_{\parallel,1}$. Note the different scales in **c**, **d**

phase, which revealed a less steep dispersion of its TSS and another E_D[39]. We ascribe this discrepancy to the known, strong sensitivity of the TSS to details of GST's atomic structure[34–39]. However, besides these remaining questions, both, the strong spin polarization close to the VB maximum and the linear dispersion within the bulk band gap are compatible with a TSS. This corrobarates the previous conjecture of a topologically inverted band structure of metastable GST-225[39].

Possible contribution of the topological surface state to conductivity. The possible presence of a TSS at E_F^{PES}, naturally protected from backscattering[54–56], raises the question whether it would contribute significantly to the conductivity. To answer this, we firstly compare the charge carrier density of the presumable TSS $n_{2D,TSS}$ with the measured charge carrier density of the epitaxial film, after projecting to 2D according to $n_{2D,H} = n_{eff,H} \cdot d$ (d: film thickness). The latter varies between $n_{2D,H} = 7 \times 10^{18}$ m^{-2} (film of largest conductivity) and $n_{2D,H} = 3 \times 10^{17}$ m^{-2} (Table 1). For the non-degenerate 2D band of a linearly dispersing TSS, we have[46]:

$$n_{2D,TSS} = \frac{k_F^2}{2\pi}. \quad (14)$$

A reasonable assumption for k_F results from extrapolating the fitted linear dispersion of Fig. 5c to E_F^{PES} leading to $|k_F| = 6 \times 10^8$ m^{-1}. An upper estimate is $|k_F| = 1.7 \times 10^9$ m^{-1}, i.e., the $k_\parallel$ value of the spin polarized state at the VB maximum. Hence, we get $n_{2D,TSS} \simeq 6 \times 10^{16}$ m^{-2}, respectively $n_{2D,TSS} \lesssim 5 \times 10^{17}$ m^{-2}.

Comparing with the sample exhibiting $n_{eff} \simeq n_{eff,H}$ ($n_{2D,H} = 7 \times 10^{18}$ m^{-2}), $n_{2D,H}$ is more than an order of magnitude larger than $n_{2D,TSS}$. We conclude that the charge carrier density is dominated by the bulk VB.

However, the mobility of a TSS (μ_{TSS}) could be much larger than the mobility of the bulk VB (μ_{bulk}). Such a TSS conductivity dominates, if $\mu_{TSS}/\mu_{bulk} > n_{2D,bulk}/n_{2D,TSS}$ ($n_{2D,bulk}$: charge carrier density in the bulk VB after 2D projection). Within the two band model, we have[46]

$$n_{2D,H} = \frac{n_{2D,TSS}^2 \cdot \mu_{TSS} + n_{2D,bulk}^2 \cdot \mu_{bulk}}{n_{2D,TSS} \cdot \mu_{TSS} + n_{2D,bulk} \cdot \mu_{bulk}} \quad (15)$$

$$\sigma_{xx} = \left(n_{2D,TSS} \cdot \mu_{TSS} + n_{2D,bulk} \cdot \mu_{bulk}\right) \cdot \frac{e}{d}. \quad (16)$$

We evaluate these equations for the sample with $n_{eff} \simeq n_{eff,H}$ ($\sigma_{xx} = 6 \times 10^4$ S m^{-1}) using the assumption of a linearly dispersing TSS down to E_F^{PES} ($n_{2D,TSS} = 6 \times 10^{16}$ m^{-2}). We solve Eq. (15) and $n_{2D,TSS} \cdot \mu_{TSS} \gtrsim n_{2D,bulk} \cdot \mu_{bulk}$ for the three remaining unknowns (μ_{TSS}, μ_{bulk}, $n_{2D,bulk}$) leading to $\mu_{TSS} \gtrsim 0.1$ m^2 (Vs)$^{-1}$. The threshold for dominating μ_{TSS} is even lower for the other samples (Table 1). We moreover assume that only the surface contains a highly mobile TSS. In turn, the threshold for dominating μ_{TSS} has to be divided by two, if the interface to the Si(111) contains a TSS with the same $n_{2D,TSS}$ and μ_{TSS}. For comparison, the record mobilities found for TSS in other systems (Bi_2Se_3, $BiSbTeSe_2$) are $\mu_{TSS} \simeq 1$ m^2 (Vs)$^{-1}$ [40,41], i.e., significantly larger than the threshold.

We conclude with the encouraging possibility to prepare highly mobile, metastable GST-225 films, noting that polycrystalline films exhibit $\sigma_{xx} < 6400$ S m^{-1} [22], which is an order of magnitude lower than for our best epitaxial film. Thus, one might boost the GST-225 conductivity by the combination of epitaxial films and adequate interface design leading to optimized TSS mobility[40,41]. This could be exploited within innovative devices combining the fast[7,8] and energy efficient[9] phase change with ultrahigh mobility of the on-state.

Discussion

We have mapped the 3D electronic bulk band structure $E(\mathbf{k})$ close to E_F of epitaxial GST films in the metastable rock salt phase and have correlated the results with magnetotransport data of identically prepared samples. The constant energy surfaces of the valence band close to E_F are hexagonal tubes with little dispersion along k_z, the direction perpendicular to the chemically distinct layers. The valence band maximum is about 100 meV below E_F, such that only the tails of the disorder broadened $E(\mathbf{k})$ states contribute to the conductivity. This is in line with the measured charge carrier densities from Hall measurements. We use the mapped band structure in combination with magnetotransport to determine the elastic scattering time (3 fs) and the mean free path (0.4 nm), the former being compatible with the peak widths found in ARPES.

Our detailed modeling reveals that variations of the band structure across the BZ. i.e., different band curvatures and peak broadenings, modify the deduced scattering time and average mean free path by about 40%, such that simplified models, as typically used for the interpretation of magnetotransport data, cannot provide a better accuracy.

Besides, we find a linearly dispersing state within the bulk band gap which might have a topological origin. We estimate that this state would dominate the longitudinal conductivity at a mobility above 0.1 m^2 $(Vs)^{-1}$, which is lower than the best mobilities of topological surface states so far ($\mu \simeq 1$ m^2 $(Vs)^{-1}$)[40,41]. Currently, topological conductivity is not expected to be dominant, but by surface or interface optimization one might exploit it in future GST devices providing an ultrahigh mobility on-state.

Methods

Sample preparation. The GST films are grown by MBE at base presure 10^{-8} Pa on a Si(111) substrate using elementary sources of Ge, Sb, and Te and a substrate temperature of 250 °C. The growth rate was 0.05 ± 0.02 nm s^{-1} and the pressure increased to 2×10^{-7} Pa during growth. XRD reveals that the films grow epitaxially in the single crystalline, metastable rock salt phase with [111] surface. The surface is Te terminated as evidenced by DFT calculations (not shown). The film thickness is determined by XRD fringes or by X-ray reflectometry to be 25, 18, and 13 nm for the samples used for ARPES, 2P-ARPES and S-ARPES, respectively. Twin domains are found, i.e., adjacent areas of ABC and CBA stacking of the hexagonal layers[39]. A peak indicating the formation of a vacancy layer is observed by XRD, hinting to more ordered samples than in the purely disordered rock salt phase[20]. The XRD data recorded after the ARPES measurements show variations in the (222) peak position by up to 1.5%[20] and in the height of the vacancy layer peak by 15–25%. However, the ARPES data of these samples are quite similar, i.e., peak positions of the VB vary by less than the peak widths. Samples are transferred in UHV between the MBE and the three different analyzing ARPES systems using a UHV shuttle with background pressure of $p = 5 \times 10^{-10}$ mbar. This prevents oxidation and surface contamination as cross-checked by X-ray photoelectron spectroscopy (XPS), such that no further preparation steps are required. The UHV transfer is crucial, since surface oxidation starts already at ~1 Pa · s of O_2[29].

Photoelectron spectroscopy. The ARPES measurements of the valence band are recorded at a sample temperature $T = 300$ K at BESSY II (beam line UE112-lowE-PGM2 (1^2)) using a Scienta R8000 analyzer with energy resolution 20 meV and angular resolution 0.2–0.3°. Linearly p-polarized light with photon energies $h\nu =$ 16–31 eV and an incidence angle of ~45° is applied, which enabled a three-dimensional mapping of the band structure in momentum space (k_x, k_y, k_z). The Fermi energy E_F^{PES} of the ARPES setup has been determined on polycrystalline Cu with 5 meV precision.

The data set contained $998 \times 666 \times 49 \times 29$ pixels, i.e., 998 different photoelectron energies E_{kin}, 666 different azimuthal angles ϕ, 49 polar angles θ, and 29 photon energies $h\nu$. The energy interval $E_{kin} \in [E_F + 0.042$ eV, $E_F + 0.104$ eV] is used for background subtraction for each energy distribution curve (EDC) at a particular (ϕ, θ, $h\nu$). Subsequently, the data are smoothed along E_{kin} and ϕ by a 5-point averaging. Accordingly, the data set is reduced to $256 \times 256 \times 49 \times 29$ pixels. Finally, all EDCs are scaled to the same average value for each (ϕ, θ, $h\nu$).

In order to deduce band centers $E_{peak,j}$ ($\mathbf{k}$) of band j, MDCs and EDCs at constant $h\nu$ are extracted from the data and fitted by two or four Voigt peaks with variable intensities, widths, and relative contributions of the Gaussian and the Lorentzian. This leads to an excellent fit quality with negligible residuals as exemplarily shown in Figs. 2c, 3g, h, and 4a. The resulting up to four $(k_x, k_y)_i$ of MDC fits are then attributed to the preselected $E - E_F^{PES} = E_{peak}$, respectively, the resulting $E_{peak,j}$ of EDC fits are attributed to the preselected (k_x, k_y) values. The resulting $E_{peak,j}(k_x, k_y)$ curves deduced from the two methods vary by $\Delta k_{||} \simeq 0.01$ Å^{-1}, respectively, by $|\Delta E_{peak}| = 5$–15 meV, except for extreme k-values (see main text). The small deviations contribute straightforwardly to the error of the determined effective charge carrier densities n_{eff} and curvature parameters m^* (Fig. 4).

Displaying the upper $E_{peak,1}(k_x, k_y)$ at selected E_{peak} for different $h\nu$, as shown for energy $E_{peak} = E_F^{PES}$ in Fig. 2f, consistently reveals a minimum diameter of the resulting constant energy lines at $h\nu \simeq 21$ eV. Since DFT finds the minimum diameter of the upper VBs at the BZ boundary (e.g., Fig. 2h), we assume that the minimum at $h\nu \simeq 21$ eV corresponds to the BZ boundary in k_z direction. This assumption is used to determine the inner potential E_{inner} with respect to the vacuum level for the final state electrons in the crystal according to $E_{final} = \hbar^2|\mathbf{k}|^2/2m_e - E_{inner}$. Restricting E_{inner} between 10 and 25 eV leaves us with the only possibility of $E_{inner} = 14$ eV. However, if the minimum diameter is in the center of the BZ, we would get $E_{inner} = 20$ eV. Since these differences are not important for our main conclusions, we select the most reasonable assumption that the smallest diameter is at the BZ boundary. Using the inner potential, we calculate k_z according to $k_z = \frac{1}{\hbar}\sqrt{2m_e E_{kin}\cos(\theta)^2 + E_{inner}}$. For the CECs and CESs in Fig. 2, we use an average value of θ to relate $h\nu$ to k_z.

The ARPES data cover only 80% of the BZ, i.e., a small part in k_z direction is missing (Fig. 2e). This is due to the fact, that at lower and higher $h\nu$, the ARPES intensity drops drastically, such that fits become unreliable. However, in line with the DFT results, we do not believe that the hexagons change strongly within the remaining 20%.

Fit procedures and fit errors. All peaks of MDC and EDC curves are fitted by several Voigt peaks, i.e., by a combination of a Gaussian and a Lorentzian peak with the same maximum each. Comparing the results of MDC fits and EDC fits for energies below the VB maximum reveals only small differences between deduced $E(\mathbf{k})$ values by 0.1 nm^{-1} or 10 meV on average, except for the extreme cases $k_{||} < 0.5$ nm^{-1} and $k_{||} > 2.5$ nm^{-1} $\left(k_{||} := \sqrt{k_x^2 + k_y^2}\right)$. The small discrepancies set a lower bound for error margins.

In order to extract n_{eff} from the fitted peaks of EDCs, the peak areas of $p_j(E, \mathbf{k})$ ($j = 1, 2$) are normalized to one leading to $p_{j,norm}(E, \mathbf{k})$, from which we evaluate the relative part of the peaks above E_F^{PES} (inset of Fig. 4a), being α_j ($\mathbf{k}$), the unoccupied percentage of the corresponding $E(\mathbf{k})$ state.

The error of $\overline{m^*}$ is only slightly smaller than the error of individual m^*, being 5% on average, which is due to the considerable variation of m^* across the BZ (Fig. 4c). The deviation of individual curves from the parabola is negligible (Fig. 4b), i.e., the average energy distance of individual $E_{peak,1}$ ($\mathbf{k}$) from the parabola (≈8 meV) is less than the average fit error from the determination of $E_{peak,1}$ ($\mathbf{k}$) by Voigt fits (≈30 meV).

Spin polarized photoelectron spectroscopy. Spin resolved ARPES measurements are conducted at BESSY II, too, using the electron analyzer SPECS PHOIBOS 150 and linearly p-polarized synchrotron radiation at $h\nu = 30$ eV and incidence angle 45° at $T = 300$ K, providing an energy resolution of 100 meV and an angular resolution of 1–2°. Spin analysis is performed with a Rice University Mott polarimeter operated at 26 kV resulting in a Sherman function of $S = 0.118$.

Two photon photoelectron spectroscopy. Angle-resolved bichromatic 2P-ARPES and additional, conventional ARPES experiments are conducted using the first, third and fourth harmonic of a titanium:sapphire oscillator, i.e., $h\nu = 1.63$ eV, $h\nu = 4.89$ eV, and $h\nu = 6.2$ eV, within a home-built setup[52,58]. The repetition rate of the laser is 80 MHz and the pulse length is 166 fs. The beam is initially p-polarized with an incidence angle of 60°. The photon energy $h\nu = 1.63$ eV is used for the pump pulse followed by the probe pulse at $h\nu = 4.89$ eV, which hits the sample at a time delay Δt after the pump. Due to time restrictions, $h\nu$ of the probe pulse has not been changed such that we probe only a single k_z. The photon energy $h\nu = 6.2$ eV is used for conventional ARPES to cross check the results obtained at BESSY II. Circular polarization, necessary for circular dichroism (CD) experiments, is obtained using a $\lambda/4$ wave plate. Two-dimensional momentum distribution patterns at constant E_{kin} are recorded using an ellipsoidal 'display-type' analyzer exhibiting an energy and angular resolution of 55 meV and 3°, respectively[52,59]. The work function of GST-225 turned out to be 5.1 ± 0.1 eV leading to a strong one-photon photoemission background from the probe pulse. In order to discriminate 2P-ARPES data from this background, the intensity of measurements at $\Delta t = -2.67$ ps is subtracted from the data recorded at $\Delta t = +1.33$ ps. Subsequently, the data are normalized to compensate for inhomogeneities of the channel plates. CD intensity displays the difference of photoelectron intensity using clockwise and counterclockwise polarized probe pulses divided by the sum of the two intensities.

Magnetotransport. Magnetotransport measurements are performed ex situ. Since Hall measurements require insulating substrates while ARPES requires a conducting sample, the Hall data are from samples with lower substrate doping, but grown with identical parameters. After growth they are capped by Te to protect

from oxidation. The samples are cut in square shapes of 5×5 mm^2 and, after decapping by a HF dip, are contacted by In and Au bond wires in a four-contact van der Pauw geometry. Magnetotransport measurements are conducted at $T =$ 4–300 K, current $I = 10$ mA, and magnetic field $B = 0.25$ T perpendicular to the surface. This leads to charge carrier densities $n_{\mathrm{eff,H}}$ and longitudinal conductivities σ_{xx} as displayed in Table 1 for $T = 300$ K. It is likely that the upper 5 nm of the sample are oxidized[29,60,61] resulting in a systematic error of 25%. We find a relatively broad statistical distribution of $n_{\mathrm{eff,H}}$ and σ_{xx}, but due to correlations between the two values, the variation of the mobility $\mu = \sigma_{xx}/n_{\mathrm{eff,H}}e$ is relatively small.

Band structure calculations. Density functional theory (DFT) calculations are performed within the generalized gradient approximation. We employ the full-potential linearized augmented plane-wave method in bulk and thin-film geometry as implemented in the FLEUR code. According to ref. [30], the Petrov stacking sequence (Te-Sb-Te-Ge-Te-Vc-Te-Ge-Te-Sb-)[15] is assumed for the metastable rock salt phase by tripling the Petrov-type unit cell containing 10 layers in order to realize the ABC stacking of the rock salt phase (Fig. 1d). The resulting BZ of the unit cell of 30 layers, is a factor of five smaller in k_z direction ($\Delta k_z = 0.12$ Å^{-1}) than the BZ of the disordered metastable rock salt phase, relevant for the ARPES data (6 layers in a unit cell, Fig. 1c). Hence, we use fivefold backfolding of the experimental data (Fig. 2g) to compare with the DFT data (Fig. 2h). Additional DFT calculations are performed for disordered slabs (Fig. 1b) with methodology otherwise similar to ref. [62]. We simulate maximum disorder by occupying each cationic plane randomly with Ge:Sb:Vc in a 2:2:1 ratio. These planes are parallel to the (111) surface, and include the disordered subsurface layer, whereas the surface itself is terminated by Te[62]. Different structure models of the cationic plane were randomly generated, and after relaxation showed a standard deviation of 3 meV/atom in total energies. The computed surface energies range from 12 to 17 meV Å^{-2} in a Te-poor environment, which can well be reconciled with previous results for ideally ordered GST[62].

More details including atomic coordinates are given in Supplementary Note 4.

Data availability. The data that support the findings of this study are available from the corresponding author upon reasonable request.

Received: 12 September 2017 Accepted: 8 January 2018
Published online: 22 February 2018

References

1. Wuttig, M. & Yamada, N. Phase-change materials for rewriteable data storage. *Nat. Mater.* **6**, 824–832 (2007).
2. Wuttig, M. & Raoux, S. The science and technology of phase change materials. *Z. Anorg. Allg. Chem.* **638**, 2455–2465 (2012).
3. Tominaga, J., Kolobov, A. V., Fons, P., Nakano, T. & Murakami, S. Ferroelectric order control of the Dirac-semimetal phase in GeTe-Sb_2Te_3 superlattices. *Adv. Mater. Interfaces* **1**, 1300027 (2013).
4. Deringer, V. L., Dronskowski, R. & Wuttig, M. Microscopic complexity in phase-change materials and its role for applications. *Adv. Funct. Mater.* **25**, 6343–6359 (2015).
5. Ovshinsky, S. R. Reversible electrical switching phenomena in disordered structures. *Phys. Rev. Lett.* **21**, 1450–1453 (1968).
6. Yamada, N. et al. High speed overwritable phase change optical disk material. *Jpn. J. Appl. Phys.* **26**, 61–66 (1987).
7. Yamada, N., Ohno, E., Nishiuchi, K., Akahira, N. & Takao, M. Rapid-phase transitions of GeTe-Sb_2Te_3 pseudobinary amorphous thin films for an optical disk memory. *J. Appl. Phys.* **69**, 849–2856 (1991).
8. Loke, D. et al. Breaking the speed limits of phase-change memory. *Science* **336**, 1566–1569 (2012).
9. Xiong, F., Liao, A. D., Estrada, D. & Pop, E. Low-power switching of phase-change materials with carbon nanotube electrodes. *Science* **332**, 568–570 (2011).
10. Park, J.-B. et al. Phase-change behavior of stoichiometric $Ge_2Sb_2Te_5$ in phase-change random access memory. *J. Electrochem. Soc.* **154**, H139–H141 (2007).
11. Matsunaga, T. & Yamada, N. Structural investigation of $GeSb_2Te_4$ a high-speed phase-change material. *Phys. Rev. B* **69**, 104111 (2004).
12. Matsunaga, T. et al. Single structure widely distributed in a GeTe-Sb_2Te_3 pseudobinary system: a rock salt structure is retained by intrinsically containing an enormous number of vacancies within its crystal. *Inorg. Chem.* **45**, 2235–2241 (2006).
13. Matsunaga, T. et al. Structural characteristics of GeTe-rich GeTe-Sb_2Te_3 pseudobinary metastable crystals. *J. Appl. Phys.* **103**, 093511 (2008).
14. Da Silva, J. L. F., Walsh, A. & Lee, H. Insights into the structure of the stable and metastable (GeTe)m(Sb_2Te_3)n compounds. *Phys. Rev. B* **78**, 224111 (2008).
15. Petrov, I. I., Imamov, R. M. & Pinsker, Z. G. Electrondiffraction determination of structures of $Ge_2Sb_2Te_5$ and $GeSb_4Te_7$. *Sov. Phys. Crystallogr.* **13**, 339 (1968).
16. Kooi, B. J. & De Hosson, J. T. M. Electron diffraction and high-resolution transmission electron microscopy of the high temperature crystal structures of $Ge_xSb_2Te_{3+x}$ ($x = 1, 2, 3$) phase change material. *J. Appl. Phys.* **92**, 3584–3590 (2002).
17. Siegrist, T. et al. Disorder-induced localization in crystalline phase-change materials. *Nat. Mater.* **10**, 202–208 (2011).
18. Schneider, M. N. et al. From metastable to stable modifications - in situ laue diffraction investigation of diffusion processes during the phase transitions of $(GeTe)_n Sb_2Te_3$ ($6 < n < 15$) crystals. *Chem. Commun.* **48**, 2192–2197 (2012).
19. Zhang, W. et al. Role of vacancies in metal-insulator transitions of crystalline phase-change materials. *Nat. Mater.* **11**, 952–956 (2012).
20. Bragaglia, V. et al. Metal - insulator transition driven by vacancy ordering in GeSbTe phase change materials. *Sci. Rep.* **6**, 23843 (2016).
21. Subramaniam, D. et al. Scanning tunneling microscopy and spectroscopy of the phase change alloy $Ge_1Sb_2Te_4$. *Appl. Phys. Lett.* **95**, 103110 (2009).
22. Volker, H. *Disorder and electrical transport in phase-change materials* (Ph.D. thesis, RWTH Aachen University, 2013).
23. Katmis, F. et al. Insight into the growth and control of single-crystal layers of GeSbTe phasechange material. *Cryst. Growth Des.* **11**, 4606–4610 (2011).
24. Rodenbach, P. et al. Epitaxial phasechange materials. *Phys. Status Solidi-R.* **6**, 415–417 (2012).
25. Bragaglia, V. et al. Structural change upon annealing of amorphous GeSbTe grown on Si(111). *J. Appl. Phys.* **116**, 054913 (2014).
26. Cecchi, S. et al. Improved structural and electrical properties in native Sb_2Te_3/$Ge_xSb_2Te_{3+x}$ van derWaals superlattices due to intermixing mitigation. *APL Mater.* **5**, 026107 (2017).
27. Mitrofanov, K. V. et al. Subnanometre resolution of atomic motion during electronic excitation in phase-change materials. *Sci. Rep.* **6**, 20633 (2016).
28. Bragaglia, V. et al. Far-infrared and raman spectroscopy investigation of phonon modes in amorphous and crystalline epitaxial GeTe-Sb_2Te_3 alloys. *Sci. Rep.* **6**, 28560 (2016).
29. Yashina, L. V. et al. X-ray photoelectron studies of clean and oxidized α-GeTe (111) surfaces. *J. Appl. Phys.* **103**, 094909 (2008).
30. Sun, Z., Zhou, J. & Ahuja, R. Structure of phase change materials for data storage. *Phys. Rev. Lett.* **96**, 055507 (2006).
31. Wang, Y. & Gedik, N. Circular dichroism in angle-resolved photoemission spectroscopy of topological insulators. *Phys. Status Solidi-R.* **7**, 64–71 (2013).
32. Scholz, M. R. et al. Reversal of the circular dichroism in angle-resolved photoemission from Bi_2Te_3. *Phys. Rev. Lett.* **110**, 216801 (2013).
33. Seibel, C. et al. The rashba-split surface state of Sb_2Te_3(0001) and its interaction with bulk states. *J. Electron Spectrosc.* **201**, 110–114 (2015).
34. Kim, J., Kim, J. & Jhi, S.-H. Prediction of topological insulating behavior in crystalline Ge-Sb-Te. *Phys. Rev. B* **82**, 201312 (2010).
35. Sa, B., Zhou, J., Song, Z., Sun, Z. & Ahuja, R. Pressureinduced topological insulating behavior in the ternary chalcogenide $Ge_2Sb_2Te_5$. *Phys. Rev. B* **84**, 085130 (2011).
36. Kim, J., Kim, J., Kim, K.-S. & Jhi, S.-H. Topological phase transition in the interaction of surface dirac fermions in heterostructures. *Phys. Rev. Lett.* **109**, 146601 (2012).
37. Sa, B., Zhou, J., Sun, Z. & Ahuja, R. Strain-induced topological insulating behavior in ternary chalcogenide $Ge_2Sb_2Te_5$. *Europhys. Lett.* **97**, 27003 (2012).
38. Silkin, I. V., Koroteev, Y. M., Bihlmayer, G. & Chulkov, E. V. Influence of the Ge–Sb sublattice atomic composition on the topological electronic properties of $Ge_2Sb_2Te_5$. *Appl. Surf. Sci.* **267**, 169–172 (2013).
39. Pauly, C. et al. Evidence for topological band inversion of the phase change material $Ge_2Sb_2Te_5$. *Appl. Phys. Lett.* **103**, 243109 (2013).
40. Koirala, N. et al. Record surface state mobility and quantum hall effect in topological insulator thin films via interface engineering. *Nano Lett.* **15**, 8245–8249 (2015).
41. Xu, Y., Miotkowski, I. & Chen, Y. P. Quantum transport of two-species dirac fermions in dual-gated three-dimensional topological insulators. *Nat. Commun.* **7**, 11434 (2016).
42. Medjanik, K. et al. Direct 3d mapping of the fermi surface and fermi velocity. *Nat. Mater.* **16**, 615–621 (2017).
43. Hüfner, S. *Photoelectron Spectroscopy* (Springer, Berlin, Germany, 2003).
44. Matzdorf, R. Investigation of line shapes and line intensities by high-resolution uv-photoemission spectroscopy - some case studies on noble-metal surfaces. *Surf. Sci. Rep.* **30**, 153–206 (1998).
45. Zhang, J. et al. Band structure engineering in $(Bi_{1-x}Sb_x)_2Te_3$ ternary topological insulators. *Nat. Commun.* **2**, 574 (2011).
46. Ando, T., Fowler, A. B. & Stern, F. Electronic properties of two-dimensional systems. *Rev. Mod. Phys.* **54**, 437–672 (1982).
47. Edwards, A. H. et al. Electronic structure of intrinsic defects in crystalline germanium telluride. *Phys. Rev. B* **73**, 045210 (2006).

48. Wuttig, M. et al. The role of vacancies and local distortions in the design of new phase-change materials. *Nat. Mater.* **6**, 122–128 (2006).
49. Lee, B.-S. et al. Investigation of the optical and electronic properties of $Ge_2Sb_2Te_5$ phase change material in its amorphous, cubic, and hexagonal phases. *J. Appl. Phys.* **97**, 093509 (2005).
50. Kellner, J. *A surface science based window to transport properties: the electronic structure of Te-based chalcogenides close to the Fermi level* (Ph.D. thesis, RWTH Aachen University, Aachen, Germany, 2017).
51. Kellner, J. et al. Exploring the subsurface atomic structure of the epitaxially grown phase-change material $Ge_2Sb_2Te_5$. *Phys. Rev. B* **96**, 245408 (2017).
52. Niesner, D. et al. Unoccupied topological states on bismuth chalcogenides. *Phys. Rev. B* **86**, 205403 (2012).
53. Crepaldi, A. et al. Momentum and photon energy dependence of the circular dichroic photoemission in the bulk Rashba semiconductors BiTeX (X = I; Br; Cl). *Phys. Rev. B* **89**, 125408 (2014).
54. Hasan, M. Z. & Kane, C. L. Colloquium: topological insulators. *Rev. Mod. Phys.* **82**, 3045–3067 (2010).
55. Qi, X.-L. & Zhang, S.-C. Topological insulators and superconductors. *Rev. Mod. Phys.* **83**, 1057–1110 (2011).
56. Ando, Y. Topological insulator materials. *J. Phys. Soc. Jpn.* **82**, 102001 (2013).
57. Pauly, C. et al. Probing two topological surface bands of Sb_2Te_3 by spin-polarized photoemission spectroscopy. *Phys. Rev. B* **86**, 235106 (2012).
58. Thomann, U., Shumay, I. L., Weinelt, M. & Fauster, T. Spin splitting of image-potential states on fcc Fe/Cu(100). *Appl. Phys. B* **68**, 531–536 (1999).
59. Rieger, D., Schnell, R. D., Steinmann, W. & Saile, V. A display-type analyzer with an image-processing system for angle-resolved photoelectron spectroscopy. *Nucl. Instrum. Methods* **208**, 777–784 (1983).
60. Zhang, Z. et al. Effective method of preparation of oxide-free $Ge_2Sb_2Te_5$ surface: An x-ray photoelectron spectroscopy analysis. *Appl. Surf. Sci.* **256**, 7696 (2010).
61. Gourvest, E. et al. Impact of oxidation on $Ge_2Sb_2Te_5$ and GeTe phase-change properties. *J. Electrochem. Soc.* **159**, H373–H377 (2012).
62. Deringer, V. L., Lumeij, M. & Dronskowski, R. Ab initio modeling of α-GeTe (111) surfaces. *J. Phys. Chem. C* **116**, 15801–15811 (2012).
63. Nonaka, T., Ohbayashi, G., Toriumi, Y., Mori, Y. & Hashimoto, H. Crystal structure of GeTe and $Ge_2Sb_2Te_5$ meta-stable phase. *Thin Solid Films* **370**, 258–261 (2000).

Acknowledgements

We gratefully acknowledge helpful discussions with H. Bluhm, M. Wuttig, and C.M. Schneider, as well as financial support by the German Science Foundation (DFG): SFB 917 via Project A3, SPP 1666 (Topological Insulators) via Mo858/13-1, and Helmholtz-Zentrum Berlin (HZB). V.L.D. was supported by the German Academic Scholarship Foundation. Computing time was provided to G.B. by the Jülich-Aachen Research Alliance (JARA-HPC) on the supercomputer JURECA at Forschungszentrum Jülich.

Author contributions

M.M. provided the idea of the experiment. J.K., M.L., and C.P. carried out all (S)ARPES experiments under the supervision of E.G., J.S.-B., O.R., and M.M.. S.O., J.K., P.K., and P. B. performed the 2P-ARPES measurements under the supervision of T.F.. J.E.B., R.N.W., S.C., and V.B. grew the samples via MBE, supervised by R.C.. V.B. performed the electrical transport measurements also supervised by R.C.. G.B. provided the DFT calculations for comparison to the ARPES data. V.L.D. and R.D. performed the additional DFT modeling of the disordered, metastable surfaces. M.L., J.K., and S.O. evaluated the experimental data. M.L., M.M., and J.K. derived the models for the interpretation of the data as discussed in the manuscript. M.M., M.L., and J.K. wrote the manuscript containing contributions from all co-authors.

Additional information

Supplementary information accompanies this paper at https://doi.org/10.1038/s42005-018-0005-8.

Competing interests: The authors declare no competing financial interest.

Reprints and permission information is available online at http://npg.nature.com/reprintsandpermissions/

Publisher's note: Springer Nature remains neutral with regard to jurisdictional claims in published maps and institutional affiliations.